Design and experimetal tests of a flexible wing of high aspect ratio for investigating flutter mechanisms

Cyrille Stephan, Xavier Amandolese

International Forum on Aeroelasticity and Structural Dynamics
IFASD 2024
17-21 June 2024, The Hague, The Netherlands

DESIGN AND EXPERIMENTAL TESTS OF A FLEXIBLE WING OF HIGH-ASPECT RATIO FOR INVESTIGATING FLUTTER MECHANISMS

Cyrille STEPHAN[1] **and Xavier AMANDOLESE**[2]

[1]ONERA
The French Aerospace Lab, CHATILLON, France
cyrille.stephan@onera.fr

[2]LMSSC
Conservatoire National des Arts et Métiers, PARIS, France
xavier.amandolese@lecnam.net

Keywords: Structural dynamics, aeroelasticity, wing, flutter

Abstract: Increasing the aspect ratio of wings may have beneficial effects in terms of aerodynamics, such as a higher lift on drag ratio. However, High-Aspect-Ratio Wings (HARW) also have a natural flexibility that can make them prone to aeroelastic instabilities for specific flight conditions. Unfortunately, computing the flutter-free domains of these HARWs is tricky due to the onset of nonlinear phenomena present for high amplitudes of wing deflections.

In that context, this paper presents the study of a taut-strip flexible wing model, particularly designed to experience flutter in a wind tunnel at low-to-moderate Reynolds numbers. The objective was to keep the structural complexity as low as possible, while exhibiting fluid-structure interactions typically observed for these types of wings. The choice of structural design was based on the numerical prediction coming from a low-order aeroelastic model combining beam theory and simplified aerodynamics.

Thanks to dynamical tests in laboratory, structural parameters (inertia, stiffness, damping coefficients) were used to update the numerical model. Using this linear model, a flutter involving a coupling between the 2nd bending mode and the 1st torsion mode was expected in the velocity range of the wind tunnel. Wind tunnel tests however show an earlier flutter bifurcation involving flapwise, chordwise and torsion motions, for which the route to flutter and post-critical limit-cycle oscillations have been measured by non-contact techniques.

1 INTRODUCTION

High aspect-ratio wings are receiving particular interest in recent years, because they may have less drag in flight, which leads to increasingly widespread use for aircraft and UAVs. However, their natural low flexibility can also induce aeroelastic effects that are difficult to predict. Indeed, structural deformations under loading are quickly high, both statically and possibly dynamically, which makes the computations of fluid-structure interactions much more complex [1].

To fully understand the possible fluid-structure interactions that can appear and endanger aircraft structures, it is useful to rely on simple wing models, representative of the phenomena

that could appear in flight [2, 3]. Here the idea was to design and to test a model of a flexible wing with a high aspect-ratio, in order to study its aeroelastic instabilities in a wind tunnel, and to analyze its behaviour using a relatively simple mathematical model. More specifically, the objectives were to observe and to analyze the route to instabilities, and during the post-critical regime to measure the evolution of limit-cycle oscillations (LCOs), with particular emphasis on the evolution of the aeroelastic modal shapes.

This paper presents the mathematical model and the design of a high aspect-ratio wing model. The experimental results coming from a wind-tunnel campaign show the evolution of its main modes with respect to wind speed, based on cameras measurement, revealing the onset of aeroelastic instabilities.

2 MATHEMATICAL MODEL

2.1 Beam equations of motion

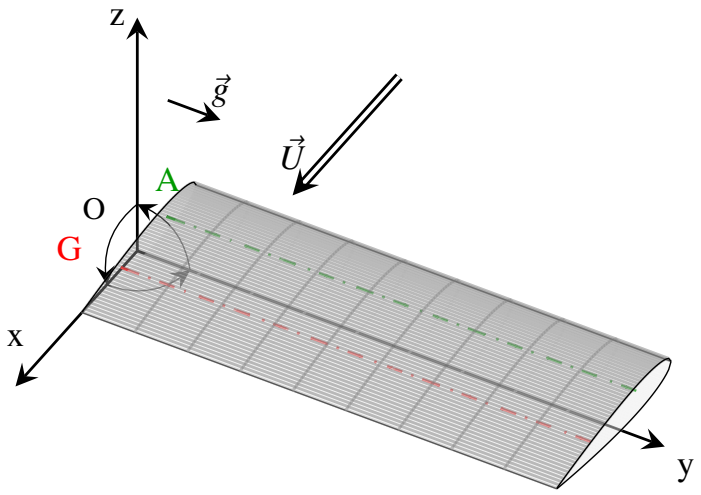

Figure 1: Schematic representation of the wing

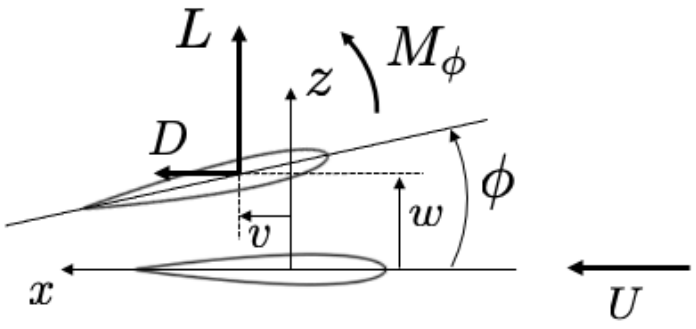

Figure 2: Degrees of freedom

The mathematical model presented in Fig. 1 and 2 was chosen to simulate the motions of the wing along three degrees of freedom : the deflection normal to the chord w, the deflection in-plane to the chord v and the torsion deflection ϕ. The deflection of the wing along its span axis y is assumed to be very small and is neglected.

The structural model is derived from the one reported in Hodges and Dowell ([4]) for a uniform, untwisted elastic wing. Neglecting cross-sectional warping, the rotary inertia effects in both bending due to the tip mass, and eccentricity in the tip mass relative to the elastic axis, the

equations of motion are

$$\begin{aligned}
\left(m + M_t\delta_y\right)\ddot{v} + C_v\dot{v} + \left(EI_z v''\right)'' &= \frac{\mathrm{d}F_v}{\mathrm{d}y} \quad (1)\\
\left(m + M_t\delta_y\right)\ddot{w} + C_w\dot{w} + \left(EI_x w''\right)'' - S_\phi\ddot{\phi} &= \frac{\mathrm{d}F_w}{\mathrm{d}y} \quad (2)\\
\left(I_\phi + I_{t,\phi}\delta_y\right)\ddot{\phi} + C_\phi\dot{\phi} - \left(GJ\phi'\right)' - S_\phi\ddot{w} &= \frac{\mathrm{d}M_\phi}{\mathrm{d}y}
\end{aligned}$$

with $\delta_y = \delta\left(y - L_w\right)$ [2].

EI_x is the flap bending rigidity, EI_z the chordwise bending rigidity, GJ the torsional rigidity, m the mass per unit length, I_ϕ the moment of inertia. M_t and $I_v, I_w, I_{t,\phi}$ are respectively the additional mass and the inertial terms at the wing tip. $S_\phi = me$ is a coupling coefficient with e is the distance between the line of mass center (G) and the wing elastic axis center. θ_0 is the pitch angle (angle of attack) at the root of the wing model. C_v, C_w et C_ϕ are the structural damping coefficients. Finally, $\mathrm{d}F_v/\mathrm{d}y$, $\mathrm{d}F_w/\mathrm{d}y$ and $\mathrm{d}M_\phi/\mathrm{d}x$ are the forces and moment distributed over the entire wing surface.

2.2 Solving the system using a Galerkin type approach

Equations are numerically solved using a Galerkin type approach [5, 2]. Deflections v, w and ϕ are expressed in series form as follows

$$\begin{aligned}
v\left(y,t\right) &= \sum_{i=1}^{n_v} f_{v,i}\left(y\right) q_{v,i}\left(t\right)\\
w\left(y,t\right) &= \sum_{i=1}^{n_w} f_{w,i}\left(y\right) q_{w,i}\left(t\right) \quad (3)\\
\phi\left(y,t\right) &= \sum_{i=1}^{n_\phi} f_{\phi,i}\left(y\right) q_{\phi,i}\left(t\right)
\end{aligned}$$

where $\left\{f_{v_i}\left(y\right), f_{w_i}\left(y\right), f_{\phi_i}\left(y\right)\right\}$ are respectively the $n_v + n_w + n_\phi$ mode shape functions of chordwise, bending and torsion deflections.

Taking into account mass and inertia at the wing tip may be done in two ways. The first one, introduced by Dowell [6, 2], consists of using the standard cantilever beam normal mode shape functions. During this step, the terms proportional to $\delta\left(y - L_w\right)$ will add coefficients in the mass and stiffness matrices, representative of the intertial contribution of the wing tip. Another way consists of computing normal modes (frequencies, modal masses and shape functions) that are inherently dependent on these additional terms [7]. Even if these two techniques are equivalent when one considers mass and stiffness coefficients, the second approach was selected here since it enables to introduce a structural damping coefficient which has a more physical meaning; indeed, damping coefficents obtained by modal tests can be directly inserted into equations. After having projected the equations on the selected modes (details in Appendix), the following system is obtained in matrix form

$$M\ddot{q} + C\dot{q} + Kq = F_e \quad (4)$$

with $q = \left[q_{v,1} \ldots q_{v,n_v} q_{w,1} \ldots q_{w,n_w} q_{\phi,1} \ldots q_{\phi,n_\phi}\right]^T$.

2.3 Quasi-static aerodynamic model

Aerodynamic forces and moment about the elastic axis are expressed as

$$\begin{aligned}
\frac{\mathrm{d}F_v}{\mathrm{d}y} &= \frac{\mathrm{d}D}{\mathrm{d}y}\cos\left(\theta_0+\phi\right) - \frac{\mathrm{d}L}{\mathrm{d}y}\sin\left(\theta_0+\phi\right) \approx cq_D\left[c_d\left(\theta_0\right) - c_l\left(\theta_0\right)\left[\theta_0+\phi\right]\right] \\
\frac{\mathrm{d}F_w}{\mathrm{d}y} &= \frac{\mathrm{d}L}{\mathrm{d}y}\cos\left(\theta_0+\phi\right) + \frac{\mathrm{d}D}{\mathrm{d}y}\sin\left(\theta_0+\phi\right) \approx cq_D\left[\frac{dc_l}{d\alpha}\left[\theta_0+\phi\right] + c_d\left(\theta_0\right)\left[\theta_0+\phi\right]\right] \\
\frac{\mathrm{d}M_\phi}{\mathrm{d}y} &= c^2 q_D \frac{dc_M}{d\alpha}\left[\theta_0+\phi\right]
\end{aligned} \tag{5}$$

where $q_D = 1/2\rho U^2$ is the dynamic pressure, U the wind speed. The section aerodynamic coefficents c_l, c_d and c_m may be obtained by approximate models ([2]).

3 DESIGN OF THE WING

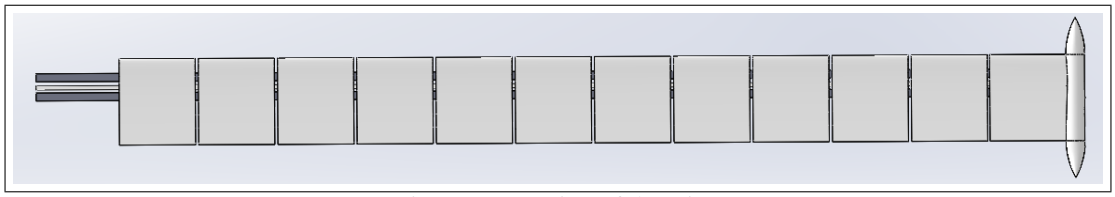

Figure 3: Drawing of the wing

The wing was designed following a taut-strip type architecture, in order to separate the structural and aerodynamic parameters as best as possible (Fig. 3). The internal structure of the wing is based on a trio of beams that ensure the stiffness in normal bending, in-plane bending and torsion.

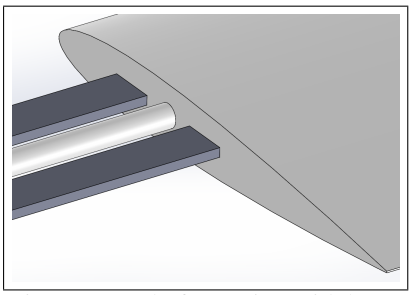

Figure 4: End of a section with beams glued

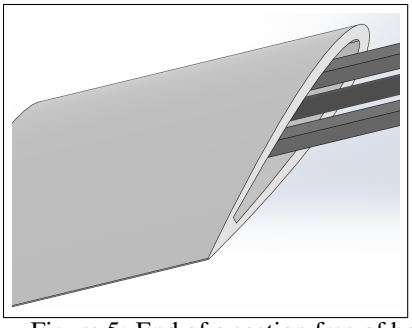

Figure 5: End of a section free of beams

These 3 beams are made by a combination of one main beam of circular section, at the wing elastic center, and two external beams of rectangular section, symetrically placed at a distance δ of the elastic center (Fig. 6). The quadratic moment of area of these 3 beams with respect to the x-axis is

$$I_x = \frac{\pi d_i^4}{64} + \frac{b_e h_e^3}{6} \tag{6}$$

Moreover, the quadratic moment of area with respect to the z-axis is given by

$$I_z = \frac{\pi d_i^4}{64} + 2\left(\delta^2 h_e b_e + \frac{h_e b_e^3}{12}\right) \tag{7}$$

Finally, as a first approximation, the global torsion stiffness J_T can be limited to the main contribution of the internal beam, which has a circular section :

$$J_T = \frac{\pi d_i^4}{32} \tag{8}$$

The two external beams are in carbon and the internal beam in aluminium.

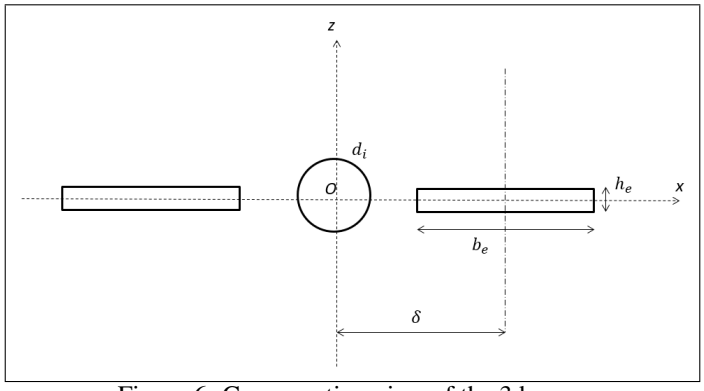

Figure 6: Cross-section view of the 3 beams

Symbol	Value
d_i	2.4 mm
δ	6 mm
h_e	1 mm
b_e	5 mm

12 sections around these beams form the aerodynamics surface of the wing. Each section is glued to the 3 beams on one of its ends (Fig. 4) and free on the other end (Fig. 5). The overall motion of this structure is assumed to be equivalent to that of a virtual global beam, created by the kinematic connection of the beams together via the different sections. Each section of NACA0012 airfoil was made by a 3D printer in resin (Fig. 7). At the wing tip, an ovoid-shaped body comprising two small masses of adjustable position makes it possible to adjust the tip inertia (Fig. 8).

The mass per unit length m is simply computed by the ratio between the total mass (beams and sections) and the overal span of the wing L_w. Inertia terms at wing tip were estimated by a numerical model in SolidWorks (computer-aided design software).

Although seemingly simplistic, the mathematical model of beams provided relevant information in order to select the parameters listed in Table 1.

In addition, it also made it possible to predict the behavior of the wing subjected to wind forces, while keeping in mind the limitations induced by the assumptions of the model, in particular on the aerodynamic part. Fig. 9 shows the evolution of the first five modes frequencies with respect to wind speed in the 0-40 Hz frequency range, by applying the mathematical model with the aeroelastic parameters of the wing. Based on these results, the first two bending modes (1B and 2B) should increase in frequency, while the first torsion mode (1T) should decrease, to

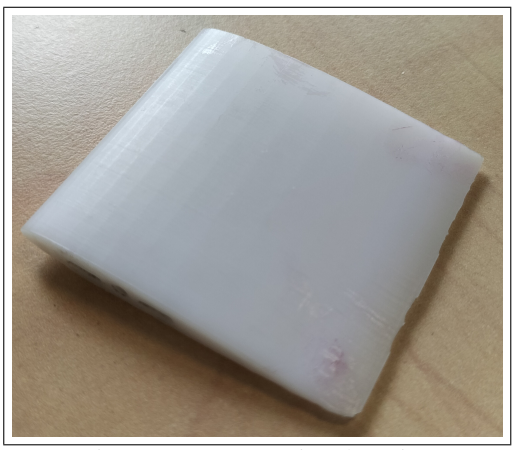

Figure 7: One 3D printed section

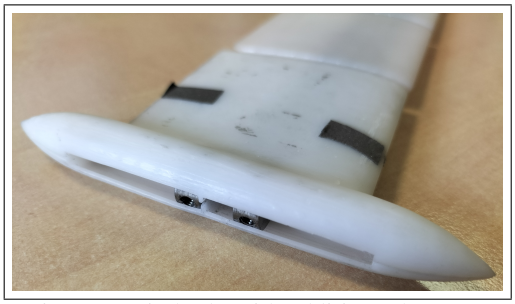

Figure 8: Tip body with additionnal masses

Table 1: Wing model data

Description	Symbol	Value
Span	L_w	600 mm (without tank)
Chord	c	54 mm
Distance between the leading edge and the elastic axis	x_{ce}	18 mm
Distance between the elastic axis and the line of center of gravity	e	4.7 mm
Mass per unit length	m	0.227 kg/m
Moment of inertia about the elastic axis per unit length	I_ϕ	kgm
Flapwise bending stiffness	EI_x	0.45 Nm^2
Chordwise bending stiffness	EI_y	29.91 Nm^2
Torsional stiffness	GJ	0.257 Nm^2
Tip mass	M_t	$4.6 * 10^{-3}$ kg
Tip moment of inertia about the elastic axis	$I_{t,\phi}$	$4.2 * 10^{-6}$ kgm^2

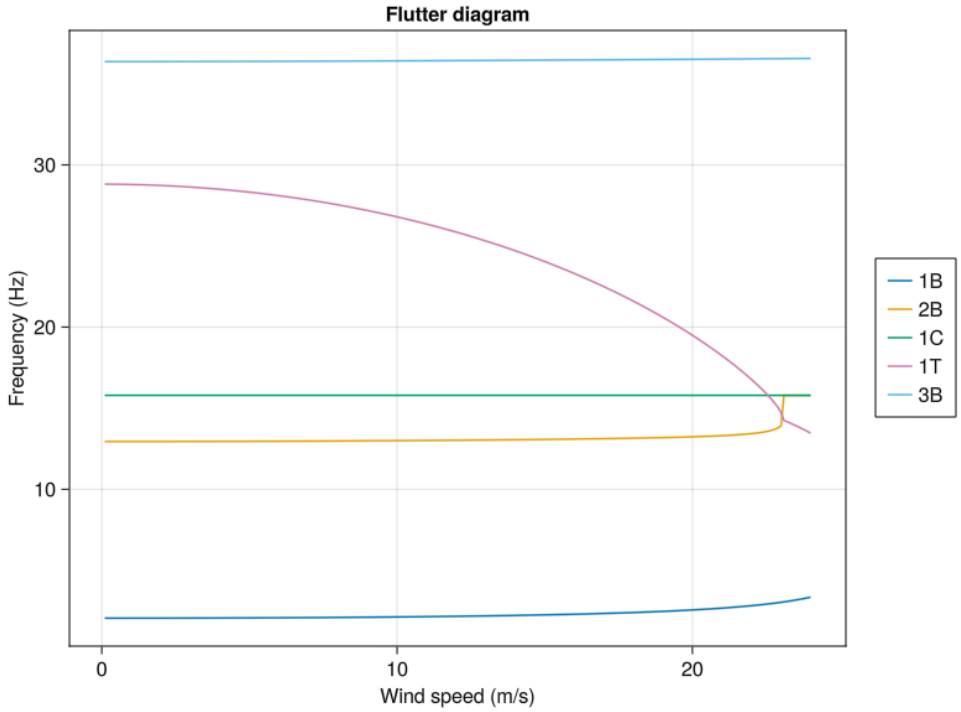

Figure 9: Evolution of the first five aeroelastic eigenfrequencies, numerical prediction using the linear model

the point that modes 2B and 1T merge, thus triggering a flutter aeroelastic instability around 23 m/s. The first in-plane mode (1C, C for chordwise), initially placed between modes 2B and 1T, is expected to be constant because negligible aerodynamic forces are generated on it. The third bending mode (3B) should also get stiffer like other bending modes, but to such a small degree that it should not be visible at these wind speeds.

4 EXPERIMENTAL RESULTS

4.1 Setup

All the tests were performed in the low speed ONERA S2L facility. The wind tunnel is an open-circuit tunnel with a hexagonal section of 0.95 m width. The maximum air speed attainable is 45 m/s. Inside the tunnel, the wing can be seen from a view from below in Fig. 10.

In order to perform the Model Deformation Measurement (MDM), two lines of three markers

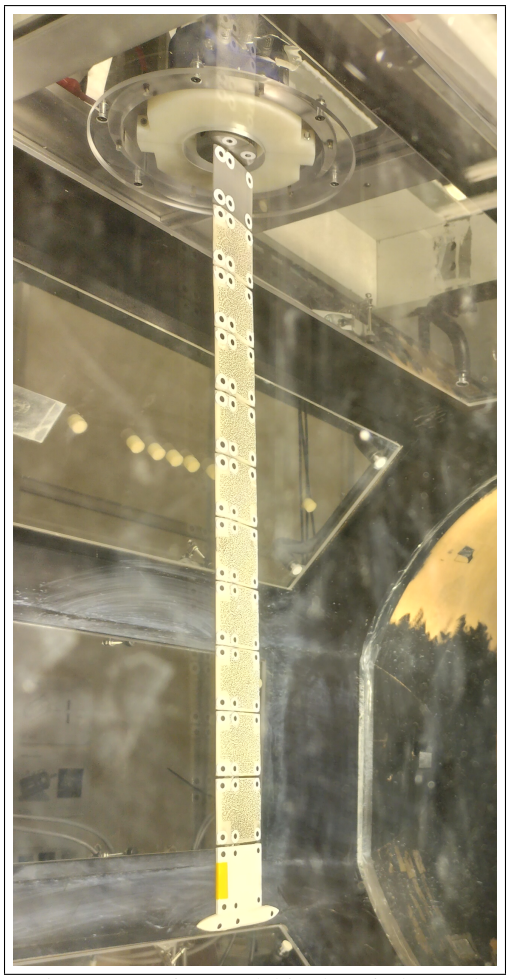

Figure 10: Wing model in the wind tunnel

were glued to monitor the displacements on the leading edge, on the line of elastic center and on the trailing edge along the wing span. The measurement system is based on two EoSens 4CXP cameras that can record 4 MP images up to 560 fps, although most of the tests were performed at 128 fps. It could be noticed that a speckle was also glued on sections, but for the moment DIC (Digital Correlation Image) was not processed.

The main components of the experimental setup at wing root are presented in Fig. 11. Thanks to a remote control servohydraulic system, the pitch angle at wing root θ_0 can be precisely controlled, both statically and dynamically. In addition, the actual θ_0 is also measured by a RVDT (Rotary Variable Differential Transformer) sensor. Forces and moments are measured by a 6DOF balance. All the parts are linked to the wind tunnel structure with a heavy support.

4.2 Modal tests without wind

Firstly, modal tests are done to get a database of the first modes, without considering fluid-structure interaction. The structure was excited by a random rotation at its base thanks to the hydraulic system, in the 0.5-45 Hz frequency range. The first 5 modes were identified by using output-only modal analysis applied on the displacements obtained by the cameras system (Fig. 12).

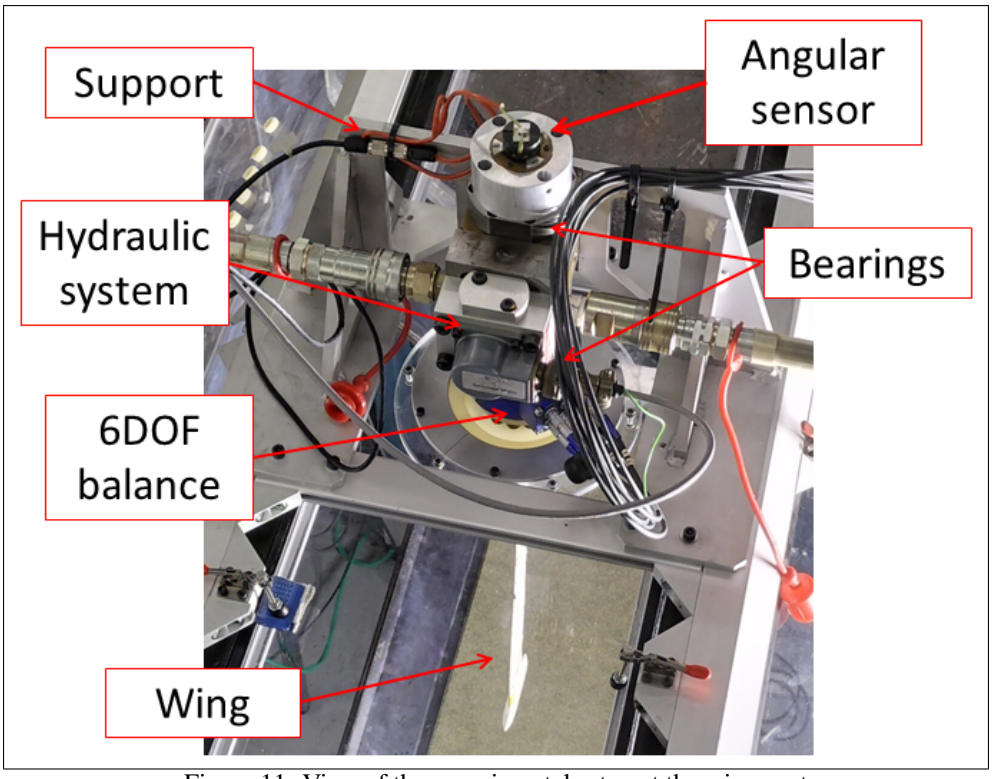

Figure 11: View of the experimental setup at the wing root

Table 2: Experimental modal parameters

Mode name	Description	f_{exp}, Hz	f_{num}, Hz	ξ_{exp}, %
1B	First normal bending	2	2.05	2.9
2B	Second normal bending	11.74	12.95	1.1
1C	First inplane bending	14.89	15.79	3
1T	First torsion	26.19	28.8	5.4
3B	Third normal bending	32.33	36.37	2

4.3 Static tests under wind loading

In a second step, static tests were performed at different wing speeds to highlight the steady response of the wing to different pitch angles at wing root. The evolution of bending moment with respect to the static pitch angle at wing root shows a good agreement between the balance and the model predictions (Fig. 13).

4.4 Dynamic tests under wind loading

Finally, a series of tests were conducted at different wind speed values in order to study the evolution of modes when the structure is subjected to aerodynamic forces and the onset of flutter. The evolution of the frequencies of the first 5 modes clearly shows that modes follow different trends from 0 to 13 m/s (Fig. 14).

As expected, the bending modes frequencies slightly increase with respect to wind speed. Mode 1B goes from 2 up to 2.11 Hz, mode 2B from 11.74 to 12.1 Hz. On the other hand, mode 3B does not show a clear trend, and is not particularly studied because its identification was difficult and does not add necessary information later.

Mode 1T frequency decreases more abruptly, from 26.19 down to 24.37 Hz. It was also ex-

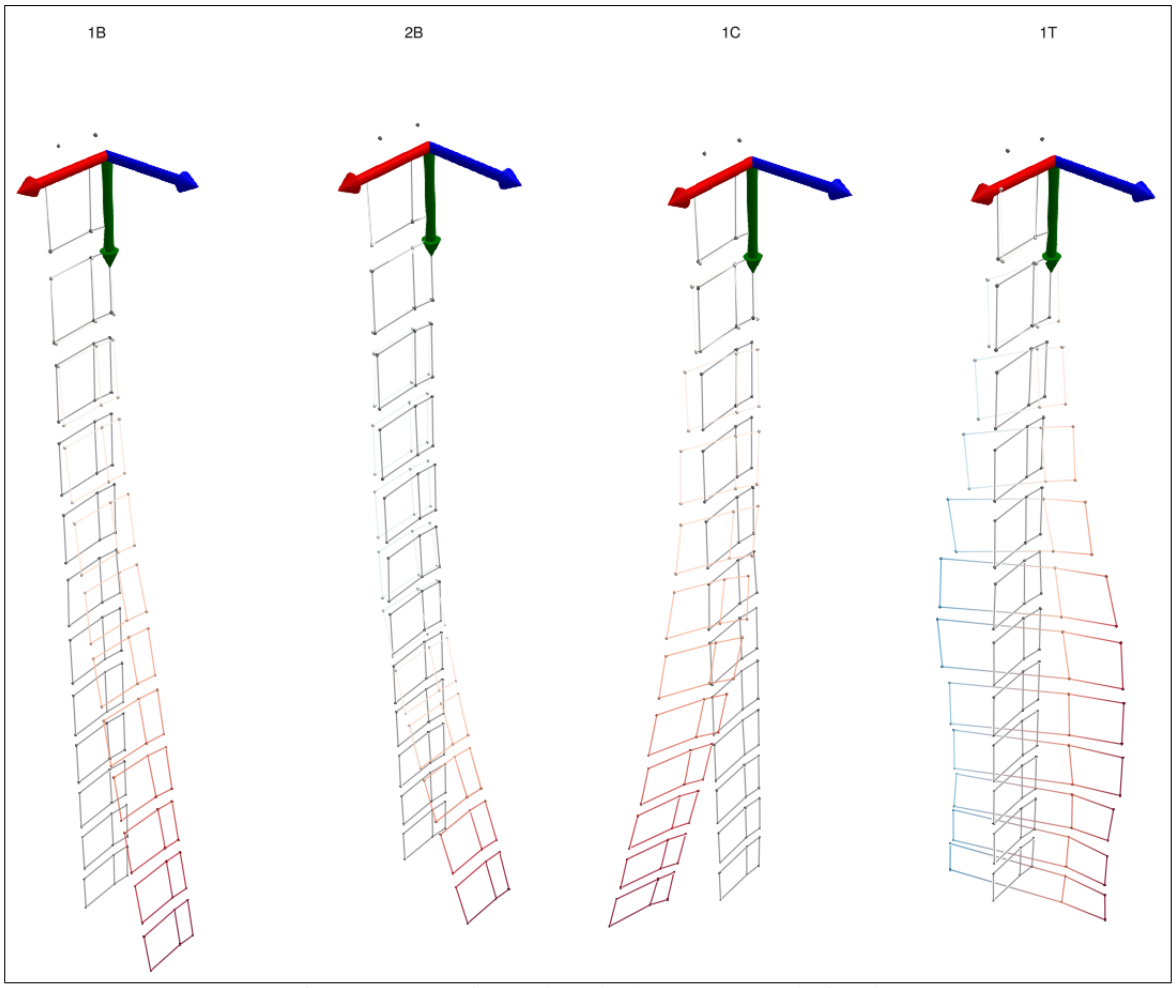

Figure 12: Experimental mode shapes (3B not depicted)

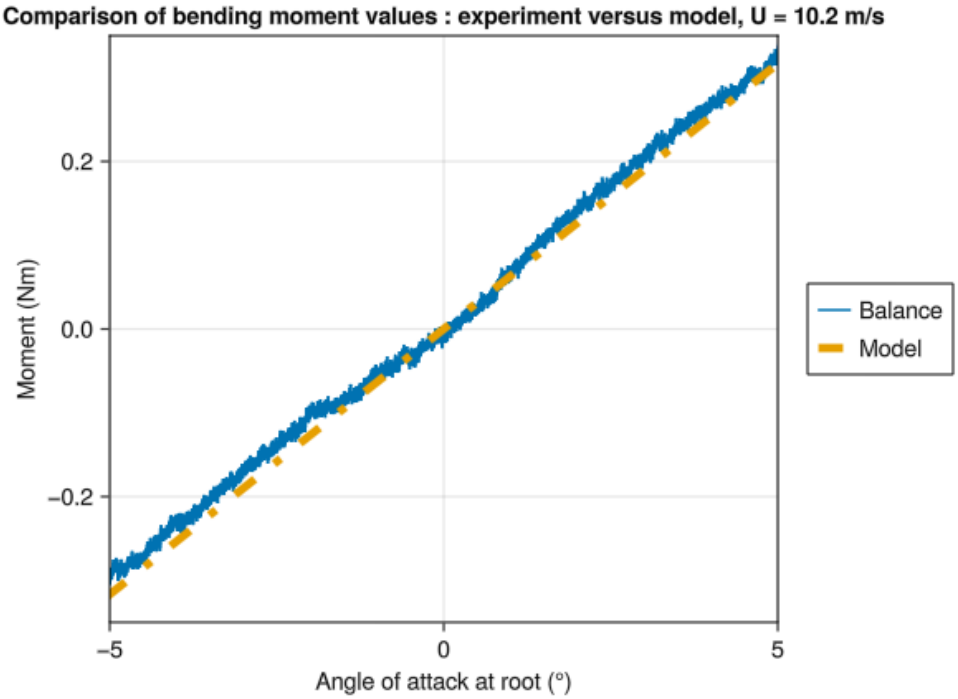

Figure 13: Bending moment at different root angles, at 10.2 m/s

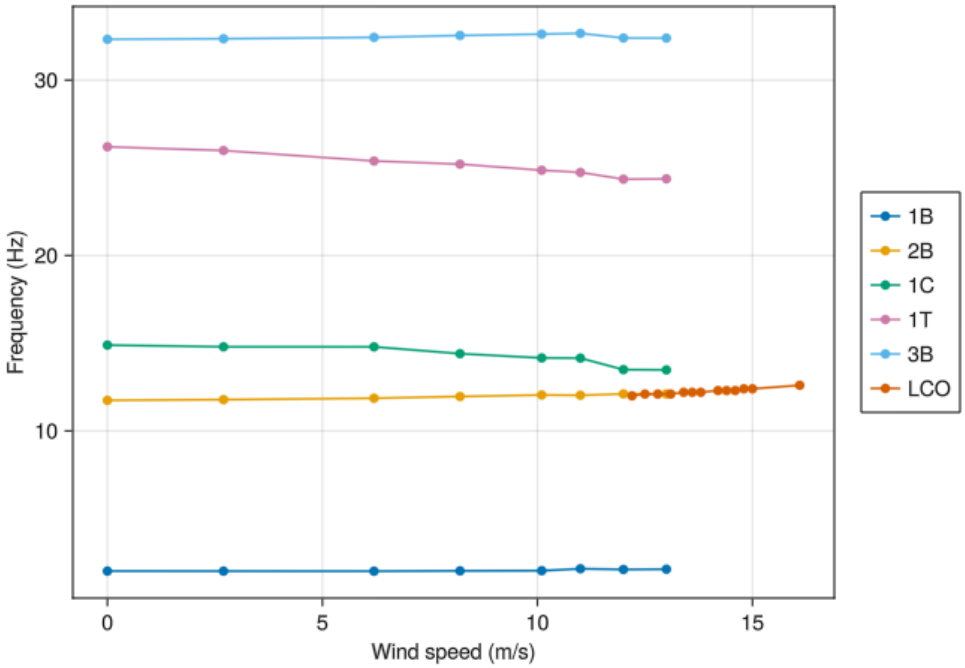

Figure 14: Evolution of the first modes and LCOs frequencies

pected since aeroelastic forces tend to bring closer bending and torsion modes, according to their respective distribution in the frequency range.

The behaviour of mode 1C is less understandable. Initially at 14.89 Hz, it would be expected not to evolve because its inplane motion should be sensitive to aerodynamic forces. Anyway, its frequency clearly decreases down to 13.48 Hz, making frequencies of 1C and 2B closer.

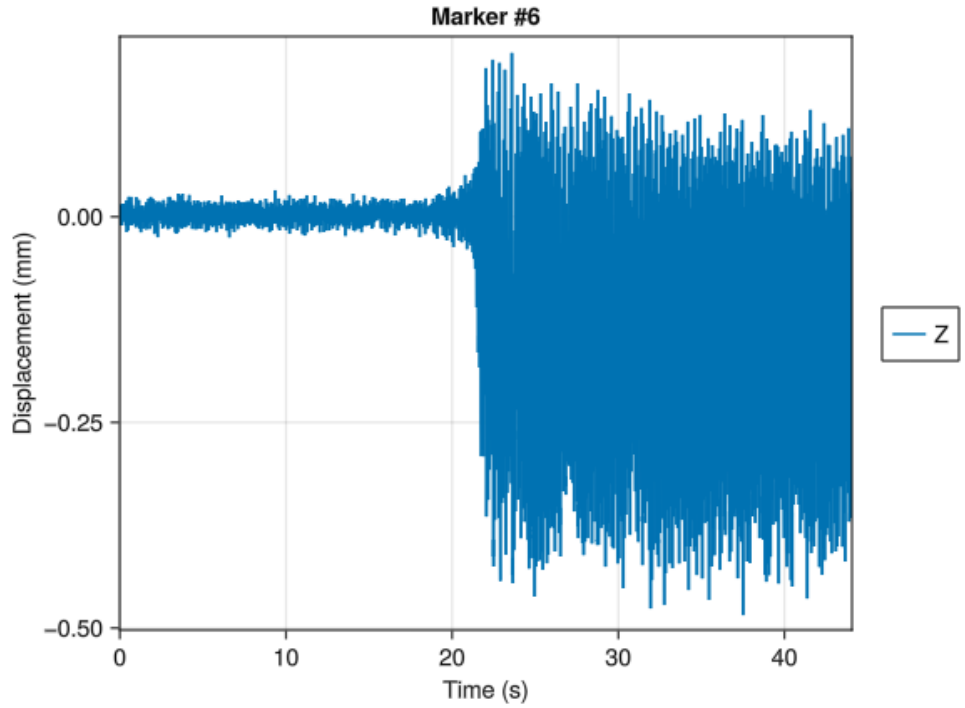

Figure 15: Onset of instability at U = 13 m/s (from a marker monitored by the cameras)

The onset of aeroelastic instability is detected at a wind speed of 13 m/s (Fig. 15). This new

regime is characterized by the emergence of LCOs of high amplitudes, thus replacing the modal behaviour that prevailed at lower speeds. The frequency of LCOs evolves gradually (Fig. 14), from 12.1 Hz at the onset up to 12.6 Hz at 16.1 m/s.

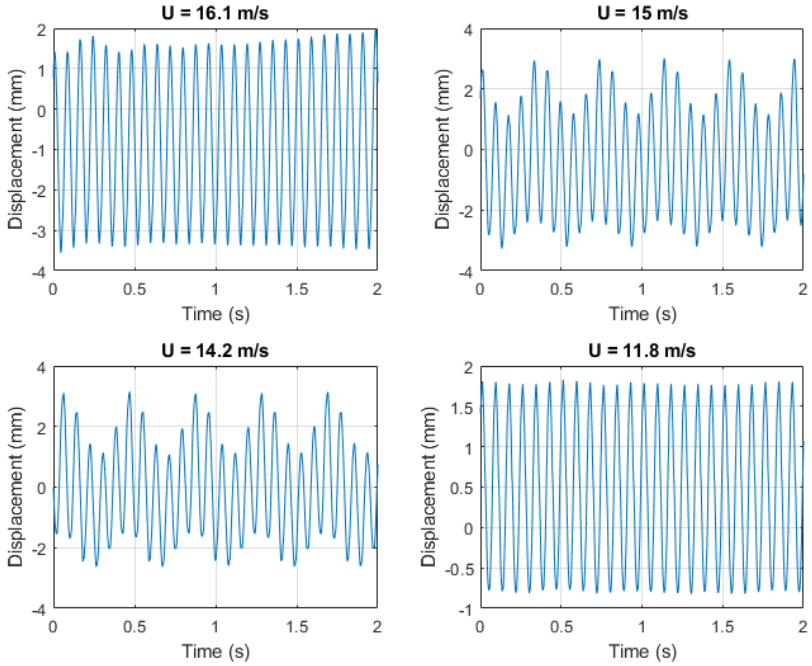

Figure 16: Wing responses at different wind speeds

The frequency content of responses also evolves strongly with respect to wind speed. Fig. 16 shows different kinds of response according to the wind speed, for a marker at 90 mm from the root, when wind speed is reduced. In this descending part, the response is almost monoharmonic at its highest level at $U = 16.1$ m/s, then becomes multiharmonic from 15 to 13 m/s, and becomes again monoharmonic at $U = 11.8$ m/s.

A detailed explanation of the physics involved in this instability is on-going. Anyway, it shall be noticed that this branch of LCOs started well below the wind speed predicted by the numerical model (23 m/s) based on a linear aeroelastic model (Fig. 9).

5 CONCLUSION

In this paper, an aeroelastic benchmarch of a flexible wing model was presented on analytical, numerical and experimental aspects. The mathematical model based on beam equations showed that it is capable of managing relatively complex physical behaviours for a low computational cost, as long as the architecture of the underlying structure remains simple. Aeroelastic instabilities were observed experimentally in this low speed wind-tunnel, thus demonstrating the presence of a branch of LCOs well below the flutter speed predicted by the numerical model. Deformations were measured by a set of cameras, then providing after operational analysis the full evolution of the first five modes (frequencies and mode shapes), and of the LCOs.

This earlier flutter bifurcation was not predicted by the linear model. From these first results, it seems that it would be a coupling between the 2nd bending mode and the 1st chordwise bending mode, with possibly also the influence of the 1st torsion mode, even if this remains to be proven. However, it is difficult to conclude without a more detailed analysis of the mechanisms highlighted. Future work will be necessary to fully understand LCOs that appear at a much

lower flutter speed than numerically predicted. Based on the full non-linear aeroelastic model from Hodges and Dowell, the non-linear interactions between the degrees of freedom will be better taken into account, and it will surely be possible to explain the appearance of this branch of LCOs and to compare the numerical predictions with experimental data.

6 APPENDIX

The equations of motion are projected on the elementary beam mode shapes

$$\sum_{i=1}^{n_v}\left(\int_0^{L_w} m f_{v,i} f_{v,j}\mathrm{d}y\right)\ddot{q}_{v,i} + C_v\sum_{i=1}^{n_v}\left(\int_0^{L_w} f_{v,i} f_{v,j}\mathrm{d}y\right)\dot{q}_{v,i} + EI_z\sum_{i=1}^{n_v}\left(\int_0^{L_w} f''''_{v,i} f_{v,j}\mathrm{d}y\right)q_{v,i} = \int_0^{L_w}\frac{\mathrm{d}F_v}{\mathrm{d}y} f_{v,j}\mathrm{d}y, \quad j = 1\ldots n_v$$

$$\sum_{i=1}^{n_w}\left(\int_0^{L_w} m f_{w,i} f_{w,j}\mathrm{d}y\right)\ddot{q}_{w,i} + C_w\sum_{i=1}^{n_w}\left(\int_0^{L_w} f_{w,i} f_{w,j}\mathrm{d}y\right)\dot{q}_{w,i} + EI_x\left(\int_0^{L_w} f''''_{w,i} f_{w,j}\mathrm{d}y\right)q_{w,i} - \sum_{i=1}^{n_\phi}\left(\int_0^{L_w} S_\phi f_{\phi,i} f_{w,j}\mathrm{d}y\right)\ddot{q}_{\phi,i} = \int_0^{L_w}\frac{\mathrm{d}F_w}{\mathrm{d}y} f_{w,j}\mathrm{d}y, \quad j = 1\ldots n_w$$

$$\sum_{i=1}^{n_\phi}\left(\int_0^{L_w} I_\phi f_{\phi,i} f_{\phi,j}\mathrm{d}y\right)\ddot{q}_{\phi,i} + C_\phi\sum_{i=1}^{n_\phi}\left(\int_0^{L_w} f_{\phi,i} f_{\phi,j}\mathrm{d}y\right)\dot{q}_{\phi,i} - GJ\sum_{i=1}^{n_\phi}\left(\int_0^{L_w} f''_{\phi,i} f_{\phi,j}\mathrm{d}y\right)q_{\phi,i} - \sum_{i=1}^{n_w}\left(\int_0^{L_w} S_\phi f_{w,i} f_{\phi,j}\mathrm{d}y\right)\ddot{q}_{w,i} = \int_0^{L_w}\frac{\mathrm{d}M_\phi}{\mathrm{d}y} f_{\phi,j}\mathrm{d}y, \quad j = 1\ldots n_\phi$$

7 REFERENCES

[1] Afonso, F., J., V., E., O., et al. (2017). A review on non-linear aeroelasticity of high aspect-ratio wings. *Progress in Aerospace Sciences*, 89, 40–57.

[2] Tang, D. and Dowell, E. H. (2001). Experimental and theoretical study on aeroelastic response of high-aspect-ratio wings. *AIAA Journal*, 39(8), 1430–1441.

[3] Avin, O., D.E., R., A., D., et al. (2022). Experimental aeroelastic benchmark of a very flexible wing. *AIAA Journal*, 60(3), 1745–1768.

[4] Hodges, D. H. and Dowell, E. H. (1974). Nonlinear equations of motion for the elastic bending and torsion of twisted nonuniform rotor blades. Tech. Rep. TN D-7818, NASA.

[5] Bisplinghoff, R. L. and Ashley, H. (1962). *Principles of Aeroelasticity*. New York: Wiley & sons.

[6] Dowell, E. H. and Traybar, J. (1977). An experimental-theoretical correlation study of non-linear bending and torsion deformations of a cantilever beam. *Journal of Sound and Vibration*, 50(4), 533–544.

[7] Meirovitch, L. (2003). *Fundamentals of Vibrations*. New York: McGraw-Hill Professional.

COPYRIGHT STATEMENT